ACSNANO

www.acsnano.org

ARTICLE

Rational Design of $Ti_3C_2T_x$ MXene Inks for Conductive, Transparent Films

Tiezhu Guo, Di Zhou,* Shungui Deng, Mohammad Jafarpour, Jonathan Avaro, Antonia Neels, Jakob Heier,* and Chuanfang Zhang*

Cite This: *ACS Nano* 2023, 17, 3737−3749

Read Online

ACCESS | Metrics & More | Article Recommendations | Supporting Information

ABSTRACT: **Transparent conductive electrodes (TCEs) with a high figure of merit (FOM_e, defined as the ratio of transmittance to sheet resistance) are crucial for transparent electronic devices, such as touch screens, micro-supercapacitors, and transparent antennas. Two-dimensional (2D) titanium carbide ($Ti_3C_2T_x$), known as MXene, possesses metallic conductivity and a hydrophilic surface, suggesting dispersion stability of MXenes in aqueous media allowing the fabrication of MXene-based TCEs by solution processing. However, achieving high FOM_e MXene TCEs has been hindered mainly due to the low intrinsic conductivity caused by percolation problems. Here, we have managed to resolve these problems by (1) using large-sized $Ti_3C_2T_x$ flakes (~12.2 μm) to reduce interflake resistance and (2) constructing compact microstructures by blade coating. Consequently, excellent optoelectronic properties have been achieved in the blade-coated $Ti_3C_2T_x$ films, *i.e.*, a DC conductivity of 19 325 S cm^{-1} at transmittances of 83.4% (≈6.7 nm) was obtained. We also demonstrate the applications of $Ti_3C_2T_x$ TCEs in transparent Joule heaters and the field of supercapacitors, showing an outstanding Joule heating effect and high rate response, respectively, suggesting enormous potential applications in flexible, transparent electronic devices.**

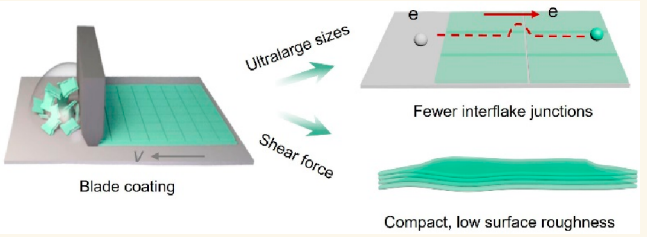

KEYWORDS: *$Ti_3C_2T_x$ MXene, transparent conductive electrodes, percolation, blade coating, supercapacitors, Joule heaters*

Transparent conductive electrodes (TCEs) are considered as a critical component in next-generation electronics, such as touch screens, liquid-crystal displays, transparent antennas, and other fields.[1−3] For TCEs, films possessing low sheet resistances (R_s) at high transparency (T) are highly desired. However, increasing T means thinning down the electrode, which inevitably decreases the number of conductive paths, leading to percolation problems and an increase in R_s.[4] At present, commercial TCEs are still dominated by indium tin oxide (ITO) due to its ultralow R_s at ultrahigh T.[1,4,5] However, the fragile nature of ITO limits its applications in flexible transparent electronics. In other words, resilient TCEs with durable flexibility that withstand repeated deformation are in high demand. Ultrathin films based on low-dimensional conductive carbon materials (i.e., carbon nanotubes, graphene), polymers (*i.e.*, PEDOT:PSS),[6−8] metals (*e.g.*, metal grids, silver nanowires),[3,9−12] and metal/nanosheet composites[13,14] are promising candidates for TCEs. To meet the minimum standard for industrial applications, TCEs require a transparency T of at least 90% and a R_s not higher than 100 Ω sq^{-1}, which corresponds to a minimum figure of merit (FOM_e) > 35, according to eq 1,[15]

$$T = \left(1 + \frac{188.5}{R_s}\frac{\sigma_{op}}{\sigma_{DC}}\right)^{-2} \quad (1)$$

where σ_{op} is the optical conductivity, σ_{DC} is the DC conductivity, and σ_{DC}/σ_{op} is defined as the FOM_e value.

Although the transmittance loss of single-layer graphene is ~2.3% (thickness ~0.34 nm),[16,17] undoped graphene TCEs are considered to possess fundamental limitations. In particular, the maximum FOM_e of liquid-exfoliated and reduced graphene oxide flakes is close to 2.[1] A quasi-continuous graphene thin film grown by chemical vapor deposition (CVD) on the other hand displays an FOM_e up to 11.[1] Despite the excellent optoelectric properties of metal grids, metallic meshes, and silver nanowires, the strict processing requirements for deposition from solution as well as the serious haze effect resulting from the disordered

Received: November 9, 2022
Accepted: January 31, 2023
Published: February 7, 2023

https://doi.org/10.1021/acsnano.2c11180
ACS Nano 2023, 17, 3737−3749

Scheme 1. Scheme of the origin of ultrahigh conductivity in MXene TCEs through blade coating.

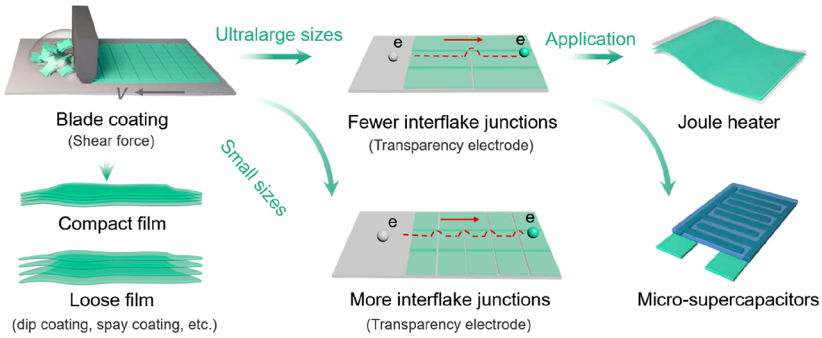

distribution of silver nanowires hinder their scalable industrial manufacturing and applications.[4] One of the key challenges for the production of TCEs with desired optoelectronic properties is the quest for electrode materials that intrinsically possess high electrical conductivity and are free of percolation problems in the high-transparency region.

MXenes are a family of 2D transition metal carbides, nitrides, or carbonitrides, generally expressed as $M_{n+1}X_nT_x$, where n = 1, 2, 3, and 4, M stands for a transition metal (Ti, Mo, Nb, V, *etc.*), X for C and/or N, and T_x for terminal groups (−O, −F, −OH, −Cl, *etc.*).[18,19] The most studied $Ti_3C_2T_x$ has been extensively researched in supercapacitors,[20,21] electromagnetic-interference shielding,[22] Na-ion batteries,[23] Joule heating,[24] and nitrogen fixation,[25] to name just a few. Andrew *et al.* demonstrated that a single layer of $Ti_3C_2T_x$ results in ∼3% loss in transmittance.[26] At present, the disadvantages of MXene-based TCEs produced by various methods include low inherent conductivity,[26−30] poorly adhering films,[31] and high surface roughness.[32,33] To the best of our knowledge, the prerequisite of high electrical conductivity at high transmittance in $Ti_3C_2T_x$ is the formation of assembled ultrathin films possessing a continuous compact morphology with few junctions. Aside from the high conductivity, the compact, highly aligned nature also endows $Ti_3C_2T_x$ films with high mechanical strength and toughness.[34,35] For example, dopamine undergoes *in situ* polymerization on the surface of $Ti_3C_2T_x$, resulting in an atomically thin polydopamine layer behaving as a binder and promoting the flake stacking/alignment.[36] Cheng *et al.* achieved densification of $Ti_3C_2T_x$ films and removal of voids by hydrogen bonding (*via* sodium carboxymethyl cellulose) and a covalent bond continuous bridging strategy (*via* borate ions), resulting in highly compact $Ti_3C_2T_x$ films with high strength.[35] However, the introduction of a nonconductive phase limits the possibilities to improve electrical conductivity. Alternatively, by utilizing shear forces to densify and align $Ti_3C_2T_x$ flakes, highly compact MXene films can be fabricated. For instance, the centripetal force from spin coating shears the solution in a way that the flakes are distributed evenly across the flat substrates, leading to a higher degree of parallel alignment than in drop-coating.[26] Compared to spin coating or dip coating, which typically lead to substantial material waste, blade coating of inks has the advantage of high material utilization and produces a higher shearing strength and anisotropy, as well as a higher degree of orientation when the blading speed is slow.[37,38]

Blade coating allows the production of films with different thickness (transparent to opaque) by simply adjusting the blade height and/or solution concentration, inducing the compact parallel arrangement of nanosheets by applying shear force.[39] Zhang *etal.* demonstrated the scalable manufacturing of opaque $Ti_3C_2T_x$ films, exhibiting high strength (∼570 MPa) and high electrical conductivity (∼15 100 S cm^{-1}) by blade coating.[34] However, reports on the fabrication of compact MXene TCEs with highly aligned flakes possessing excellent FOM_e are quite rare, to the best of our knowledge.

On top of morphology control, the electrical conductivity of $Ti_3C_2T_x$ films can also be tuned by reducing the number of interflake junctions. In general, for films produced from large-sized 2D flakes, this number can be much lower compared to films fabricated from small-sized 2D flakes at a given thickness, leading to much higher electrical conductivity in the former.[40] This highlights the importance of MXene flake size, in particular for TCEs which typically encounter percolation problems in the highly transparent region. In addition, the degree of $Ti_3C_2T_x$ flake delamination and aggregation will affect the quantity of interflake tunnelling barriers. In other words, the preparation of uniform, predominantly single-layer $Ti_3C_2T_x$ flakes with ultralarge lateral size is of significance when it comes to the realization of highly conductive $Ti_3C_2T_x$-based TCEs.

Here, our work reports blade-coated $Ti_3C_2T_x$ TCEs with compact flakes highly orientated along the substrates. The $Ti_3C_2T_x$ TCEs exhibit a record-high FOM_e without observed obvious percolation problems. We believe several factors are responsible for the state-of-the-art optoelectronic properties: (1) the large-sized $Ti_3C_2T_x$ flakes (12.2 μm) ensure a reduced quantity of interflake junctions for electron hopping, and (2) the shear force induced by blade coating guarantees a compact microstructure of large aspect ratio flakes, facilitating the electron transport among the transparent conductive films. We observe an excellent Joule-heating effect for the $Ti_3C_2T_x$ TCEs and outstanding rate performance for solid-state transparent supercapacitors, suggesting the enormous potential of our blade-coated $Ti_3C_2T_x$ TCEs in fabricating next-generation advanced transparent electronics.

RESULTS AND DISCUSSION

In this work, we employ blade coating of MXene aqueous inks to fabricate MXene TCEs. As demonstrated in Scheme 1, two aqueous inks were rationally designed enriched with large-sized flakes (lateral size up to ∼12.2 μm) and normal flakes (lateral size ∼1 μm), respectively. Detailed synthesis of MXene inks can be found in the Supporting Information. The blade-induced shear force and subsequent heat treatment enabled the $Ti_3C_2T_x$ flakes to assemble into a compact architecture with large nanosheets orientated parallel to the substrate. The highest FOM_e value we could reach with this method was 29 with a film of a thickness of ∼7 nm showing an electrical

https://doi.org/10.1021/acsnano.2c11180
ACS Nano 2023, 17, 3737−3749

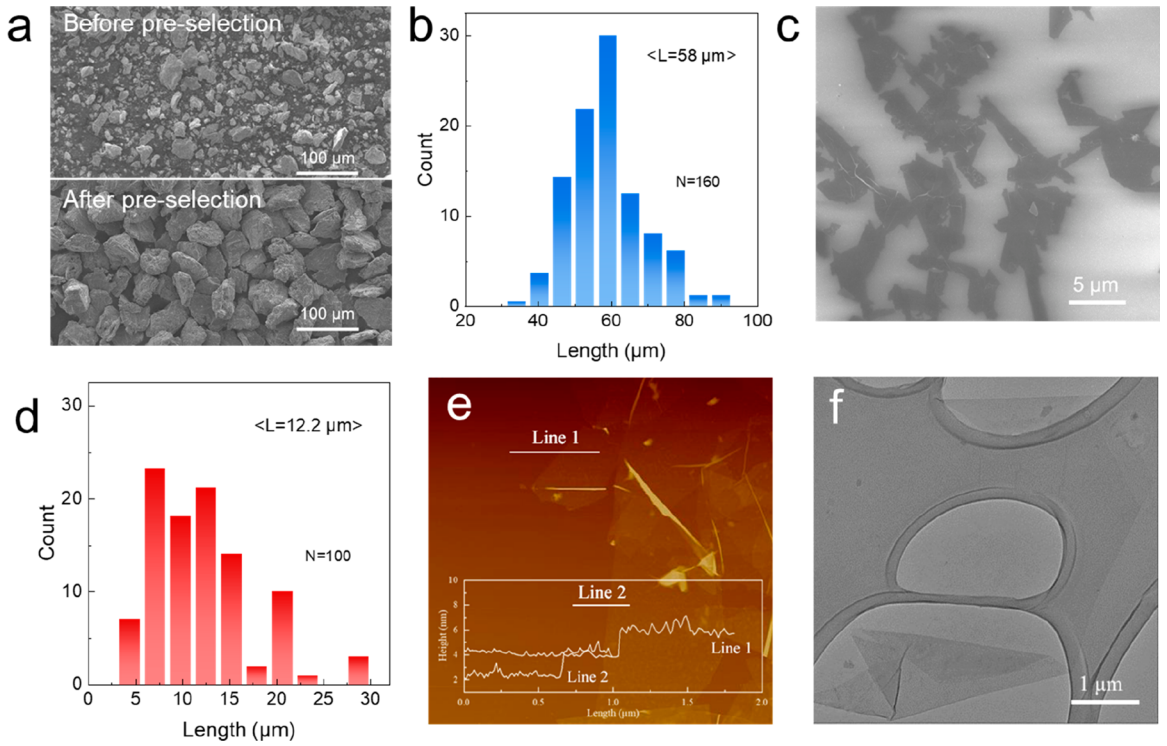

Figure 1. (a) SEM images of MAX phases before and after preselection. (b) Histogram of preselected MAX phases. SEM image (c) and the histogram (d) of $Ti_3C_2T_x$ flakes. AFM (e) and TEM (f) images of $Ti_3C_2T_x$ flakes.

conductivity of 21 750 S cm^{-1}. To the best of our knowledge, this is the highest reported value to date for $Ti_3C_2T_x$ TCEs, even higher than most opaque conductive films. The excellent optoelectronic properties of transparent MXene films ensure promising applications in transparent electronics requiring high conductivity and transmittance, such as transparent Joule heaters and solid-state micro-supercapacitors, as shown in Scheme 1.

We start by describing the formulation of high-quality MXene special inks. We preselected Ti_3AlC_2 particles of specific size from the as-received MAX phase by settling the Ti_3AlC_2 particles in water at different velocities based on Stokes' law; experimental details are shown in the Supporting Information. The MAX phase with a mean particle size of 58 μm was collected, in sharp contrast to the as-received MAX powers where a broad size distribution is observed, as shown in Figure 1a,b. The preselected Ti_3AlC_2 was etched by the optimized MILD route (24 M LiF/9 M HCl) at 50 °C for 48 h as detailed in the Supporting Information. After multiple times of washing and subsequent density gradient centrifugation, viscous aqueous inks consisting of ultralarge $Ti_3C_2T_x$ flakes with a narrow size distribution were obtained.

The successful removal of the Al element from the MAX phase and the successful preparation of $Ti_3C_2T_x$ were proven by X-ray diffraction (XRD): the characteristic peak of the Ti_3AlC_2 MAX phase located at 39° disappears; instead, the peak centering at 6.6−6.8° is observed (Figure S1).[41,42] The scanning electron microscope (SEM) image and the size histogram indicate a mean lateral size $\langle L \rangle$ of 12.2 μm in the delaminated MXene flakes, as shown in Figure 1c,d. The maximum lateral size of delaminated $Ti_3C_2T_x$ is up to 30 μm, in sharp contrast to the sonicated $Ti_3C_2T_x$ with an $\langle L \rangle$ of 1 μm (Figure S2). The thickness of the large $Ti_3C_2T_x$ flakes is 1.2−1.5 nm (Figure 1e) based on the height profile from the atomic force microscopy (AFM) measurement, consistent with previous reports of single-layer $Ti_3C_2T_x$ flakes.[43,44] The predominantly large-sized single-layer $Ti_3C_2T_x$ flake is transparent under the electron beam, possessing well-defined edges according to the transmission electron microscope (TEM) image shown in Figure 1f. The TEM image also indicates the high quality of as-delaminated flakes, as no pinholes or apparent defects are found on the flake surface (Figure S3). We believe the MXene clean surface coupled with their large lateral size is certainly beneficial for the excellent electronic conductivity, as will be discussed below.

In general, the high quality (including the transparency, homogeneity, *etc.*) of the films fabricated through blade coating is governed by various factors such as blade height, ink concentration, blade speed, and substrates properties. To obtain highly transparent (T > 80%) and uniform conductive thin films, the concentration of $Ti_3C_2T_x$ ink was kept at 2−10 mg mL^{-1}, since a too diluted solution (<2 mg mL^{-1}) leads to discontinuous thin films, while too concentrated (>30 mg mL^{-1}) ink results in opaque (T < 20%) thin films. Aside from the ink concentration, the blade height was also adjusted to obtain transparent films with desired thickness or transparency, as illustrated in Figure 2a. After blade coating, vacuum annealing at 180 °C (glass substrate) was conducted to allow the capillary force densifying the as-deposited flakes, forming interconnected, compact $Ti_3C_2T_x$ TCEs.[22] A digital photograph of a typical $Ti_3C_2T_x$ film (T = 83%) on glass substrate is shown in Figure 2b and Figure S4.

The SEM image (Figure 2c) showcases that the transparent film (T = 74%) possesses a flat smooth surface with large-sized flakes continuously and closely covering the glass substrate. We also compared SEM images of MXene TCEs from previously published works with our transparent film; it is clearly visible that our film does not show any of the sharp contrasts visible in

https://doi.org/10.1021/acsnano.2c11180
ACS Nano 2023, 17, 3737−3749

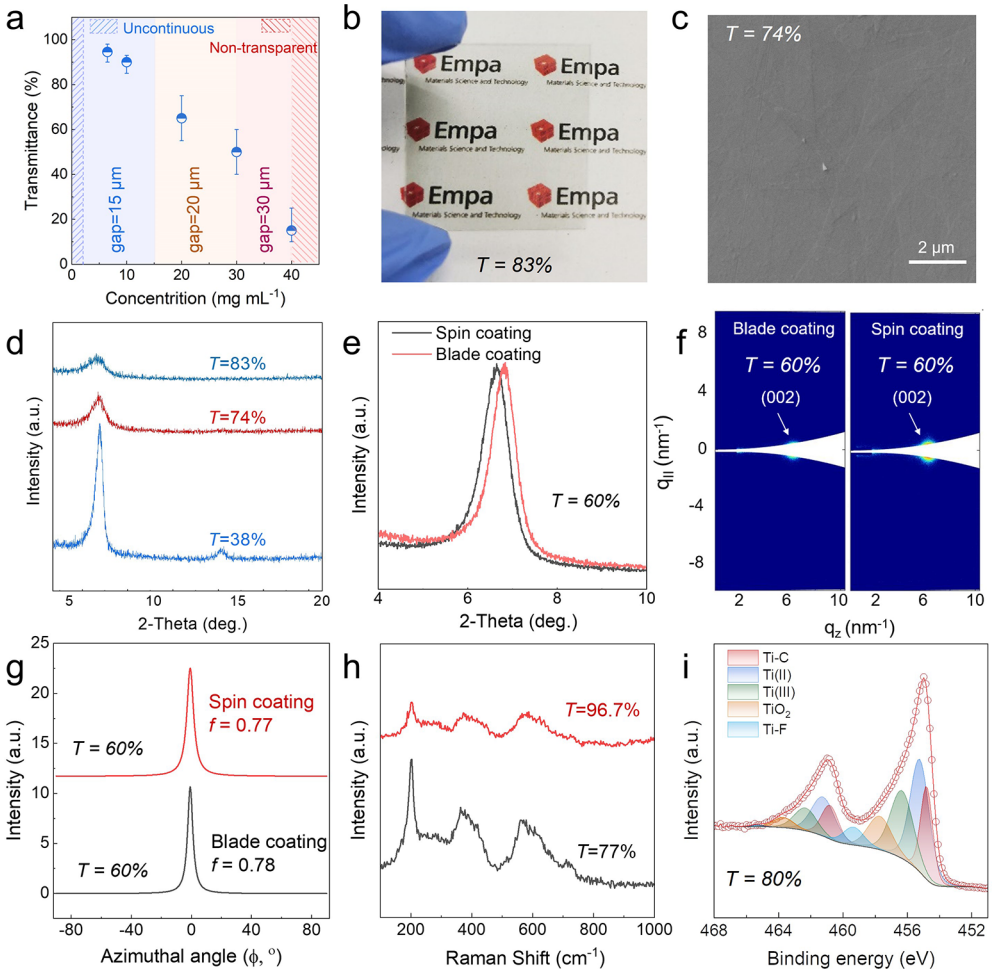

Figure 2. (a) Guiding map for MXene TCE fabrication. (b) Digital photograph of $Ti_3C_2T_x$ films from large-sized flakes on glass (T = 83%). (c) Top-view SEM images of a blade-coated $Ti_3C_2T_x$ film (T = 74%). (d) XRD patterns of various transparent films by blade coating. (e) XRD patterns of blade-coated and spin-coated $Ti_3C_2T_x$ films (T = 60%) on glass. (f) GISAXS measurement of a $Ti_3C_2T_x$ TCE (T = 60%). GISAXS detector image showing the (002) peak over q_z. (g) Lorentzian fit of the azimuthal profile for the (002) peak used to determine the Herman's degree of orientation. (h) Raman spectra of $Ti_3C_2T_x$ films with different transparency. (i) XPS spectrum of a $Ti_3C_2T_x$ film (T = 80%).

other works (Figure S5). The cross-sectional FIB-SEM image (Figure S6) reveals a flat film thickness of ~11 nm, consistent with AFM and profilometer measurements, which will be described later. To determine the alignment and compactness of the films, XRD was performed on transparent $Ti_3C_2T_x$ films with different transmittances. As shown in Figure 2d, only (00l) reflection peaks are observed in the $Ti_3C_2T_x$ thin film (T = 38%), indicating that $Ti_3C_2T_x$ flakes are highly aligned in parallel to the glass substrate. Thinning down the film to T = 74% and T = 83% leads to broader (002) peaks with much lower peak intensity, in good agreement with the literature.[45] Compared with the spin-coated film, the blade-coated film showcases a stronger (002) peak at 6.8° (spin-coating at 6.6°) and a smaller full-width-at-half-maximum of 0.56° (spin-coating, 0.61°, Figure 2e) at a given T = 60%, suggesting the $Ti_3C_2T_x$ flakes are more compact (narrower interlamellar spacing) and better aligned (better crystallinity) in the blade-coated film than those of the spin-cast counterpart. The blade-coated films with large-sized or small-sized $Ti_3C_2T_x$ flakes also showcase smaller interlayer spacings than filtered films (Figure S1).

To confirm the improved flake orientation in the blade-coated films, we employed grazing-incidence small-angle X-ray scattering (GISAXS) measurements. We compared the shape of the (002) reflection present at $q_z \sim 6.2$ nm^{-1} (Figure 2f) and fitted its azimuthal profile with Lorentzian curves (Figure 2g). The degree of orientation was calculated using the Lorentzian curve and the Hermann orientation factor (f) as previously established for MXene flakes measured in transmission mode.[34] The calculated f shows that the blade-coated film possesses a slightly higher value (0.78) than the spin-coated film (0.77). In addition, we also measured the orientation of the filtered opaque film (~1 μm) to be f = 0.63 (Figure S7), similar to the values reported by Zhang *etal.*,[34] which is significantly lower than in blade-coated transparent films. The Raman spectra of $Ti_3C_2T_x$ films with different transmittance are shown in Figure 2h; all characteristic peaks agree well with previously recorded Raman spectra of $Ti_3C_2T_x$,[44] suggesting that no oxidation was observed in the films. This is further verified by X-ray photoelectron spectroscopy (XPS), as the chemical composition and structure of the transparent film (T = 80%) are quite similar to those of nontransparent fresh MXene films (Figure 2i).[46]

Optoelectronic Properties of the $Ti_3C_2T_x$ Thin Films. As mentioned before, by adjusting factors such as ink concentration and/or blade height, films with different

https://doi.org/10.1021/acsnano.2c11180
ACS Nano 2023, 17, 3737−3749

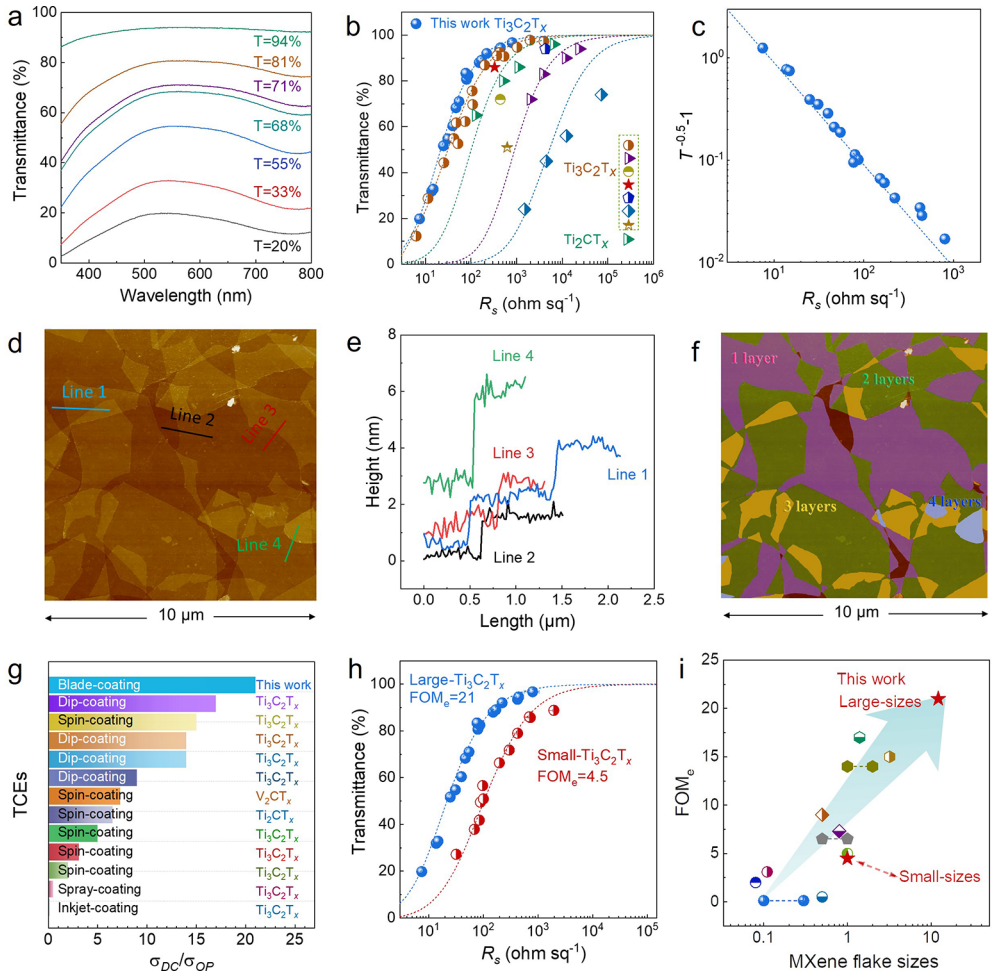

Figure 3. Optoelectronic properties of $Ti_3C_2T_x$ thin films. (a) UV−vis spectra of films with various transmittance. (b) The relationship between transmittance (T) and sheet resistance (R_s). Also included are fitting curves and (T, R_s) from literature reports. (c) $T^{-0.5} - 1$ as a function of R_s to confirm the fitting value. (d) AFM image of a $Ti_3C_2T_x$ film at T = 94% (MXene coverage 98%). (e) Height profiles of the different lines marked on (d). (f) Areas comprising different numbers of layers in (d) are shown with different colors. (g) Comparison of σ_{DC}/σ_{op} (FOM_e) in various transparent conductive MXene films; detailed values are presented in Table S2. (i) Relationship between FOM_e and MXene flake sizes.

transmittances can be obtained at ease. The UV−vis spectra showcases characteristic peaks of $Ti_3C_2T_x$ thin films in the visible region, with a broad peak in the thicker films (Figure 3a). We plotted the relationship between the sheet resistance (R_s) and transmittance (T) at 550 nm of $Ti_3C_2T_x$ thin films and fitted T as a function of R_s according to eq 1, as shown in Figure 3b. Quite interestingly, the highly transparent film (T = 96.7%) only exhibits an R_s of 800 Ω sq^{-1}, significantly lower than that of other MXene-based TCEs ($Ti_3C_2T_x$, Ti_2CT_x) with similar transmittance. Literature examples include films prepared by spin-coating Ti_2CT_x (T = 96%, 6440 Ω sq^{-1}),[33] interfacial self-assembly $Ti_3C_2T_x$ (T = 96.9%, 1623 Ω sq^{-1}),[47] and dip-coating $Ti_3C_2T_x$ (T = 94%, 4300 Ω sq^{-1}).[45] The much reduced R_s suggests the advantage of our ink design as well as methodology in thin-film fabrication. In addition, previous transparent $Ti_3C_2T_x$ MXene films based on spin-coating[28] and inkjet-printing,[29] have typically encountered percolation problems as T > 85%, best seen by the strongly deviated R_s from the fitting line.[1,4] From fitting of the entire regime, we obtained the average FOM_e value of 21 (Figure 3b), the highest reported value to date for MXenes, to the best of our knowledge (*e.g.*, $Ti_3C_2T_x$, Ti_2CT_x, V_2CT_x) thin films; detailed values are presented in Table S2. The best $Ti_3C_2T_x$ film in this work exhibits an FOM_e value of 29. Interestingly, the sheet resistance of transparent $Ti_3C_2T_x$ films is independent of film thickness, demonstrating a typical bulk-like conductivity. By fitting $T^{-0.5} - 1$ as a function of R_s, we can further confirm that the bulk-like conductivity behavior applies to the transparent $Ti_3C_2T_x$ films in the entire range of transmittance (20% < T < 94%, Figure 3c).[15] More importantly, the (R_s, T) data set of our TCEs follows the theoretical curve very well, even at high transmittance, indicative of the absence of notorious percolation problems. Specifically, we take the average value of the transmittance from five different regions as the transmittance of the TCEs, while three different surface regions were characterized by AFM, as shown in Figure 3d,e,f and Figure S8. At T = 94%, the large-sized single-layer flakes form continuous conductive pathways with a coverage of 98%, which effectively avoids the percolation problem. Clearly, the absence of percolation issues in our films guarantees their excellent optoelectronic properties. In addition, based on AFM images (Figure 3f), we could very accurately determine the average thickness of the T = 94% film. In the 10 × 10 μm area, the average film thickness is about 1.8 layers, which corresponds to about 2.2−2.7 nm (at 1.2−1.5 nm/layer). The details of the thickness calculation are presented in Table

https://doi.org/10.1021/acsnano.2c11180
ACS Nano 2023, 17, 3737−3749

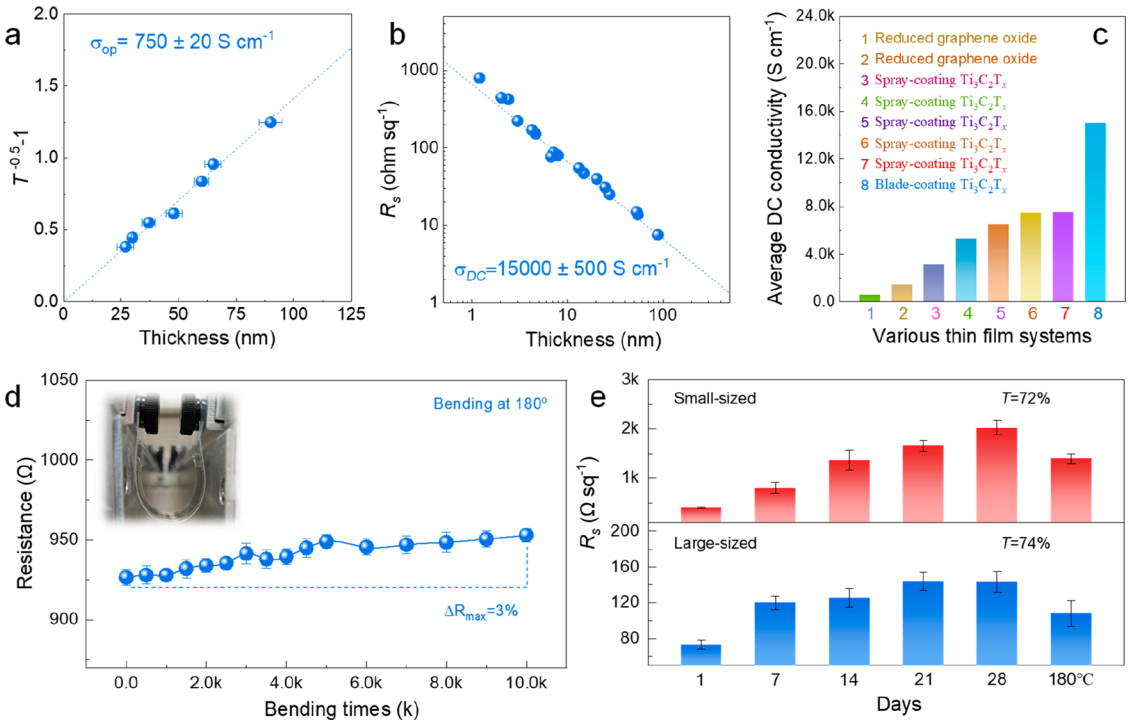

Figure 4. (a) $T^{-0.5} - 1$ as a function of thickness (t, >20 nm), to obtain the optical conductivity (σ_{op}) of $Ti_3C_2T_x$ thin films. (b) R_s as a function of t to extrapolate the average conductivity (σ_{DC}) of $Ti_3C_2T_x$ thin films. (c) Comparison of average electronic conductivity in various transparent conductive films. Detailed values are presented in Table S4. (d) Changes in resistance of TCEs after folding at 180° for 10 000 cycles. (e) R_s as a function of time under ambient conditions. The large-sized and small-sized flakes form a film with T = 74% and T = 72%, respectively.

S1. In Figure 3g, Figure S9, and Table S2, 3 we show FOM_e values of reported MXene and undoped graphene films. Obviously, the FOM_e values of our MXene films have outperformed the solution-processed 2D inks; the latter also showcases non-bulk-like behavior due to percolation effects at high transparency. Such excellent optoelectronic properties in our blade-coated transparent MXene films can be fairly attributed but are not limited to the following reasons: (1) large-sized flakes suggest fewer junctions for electron hopping; (2) compact and highly aligned morphology ensures the efficient contact for the interflakes; and (3) the high-quality MXene flakes guarantees fast electron transport. To correlate performance to size, we fabricated MXene films using conventional small-size (average size of 1 μm) $Ti_3C_2T_x$, revealing a relatively low FOM_e of 4.5 (Figure 3h), similar to the values reported previously.[27,33,48,49] A systematic comparison among various MXene TCEs reported in the literature confirms this trend: the FOM_e increases as the flake size enlarges (Figure 3i). This means that for further improving the optoelectronic performance of MXene-based TCEs, one needs to substantially boost the flake sizes, until the FOM_e reaches the plateau (theoretical limit).

As film thickness largely governs sheet resistance, an accurate measurement/prediction of thickness is important. Here we measured the thickness of films by contact profilometry when the films are thicker than 20 nm and obtain the optical conductivity, σ_{op}, using the following eq 2:[15]

$$T = (1 + 188.5\sigma_{op}t)^{-2} \quad (2)$$

where t is the thickness of films. We rearrange the above eq 2 to

$$T^{-0.5} - 1 = 188.5\sigma_{op}t \quad (3)$$

Plotting $T^{-0.5} - 1$ as a function of t gives a linear curve with a slope equal to $188.5\sigma_{op}$. As such, we prepared a series of low-transmittance films from T = 52% to T = 20% on glass substrates to measure T and t through UV−vis and contact profilometry, respectively. The σ_{op} of $Ti_3C_2T_x$ thin films is derived as 750 ± 20 S cm^{-1} (Figure 4a), which is slightly higher than that of $Ti_3C_2T_x$ (520 S cm^{-1}) from spin coating.[7] σ_{op} is controlled by the intrinsic characteristics of $Ti_3C_2T_x$ and the number of flakes per volume.[1] We suggest that the variation in σ_{op} is due to film-to-film differences in morphological properties such as surface roughness. A lower transmissivity (corresponding to a higher σ_{op}) in the blade-coated films than that of spin-coated films at a given thickness implies that blade-coated films are more compact with a larger total amount of aligned stacked flakes. This conclusion is also in line with the GISAXS result.

Based on eq 3 with a known σ_{op}, any film's thickness can be calculated from the measured T, as shown in Figure S10a. For example, the calculated film thickness of the T = 74% film (11.5 nm) is approximately the value extracted from the cross-sectional focused-ion-beam (FIB) SEM image (11 nm) and at T = 94% (2.2 nm) is approximately the average thickness of AFM characterization (2.2−2.7 nm). The results showcase that eq 3 is quite trustable in predicting the thickness of highly transparent MXene films. With the calculated thickness of all transparent films, their DC conductivity is then measured using eq 4:[7]

$$\sigma_{DC} = \frac{1}{R_s t} \quad (4)$$

https://doi.org/10.1021/acsnano.2c11180
ACS Nano 2023, 17, 3737−3749

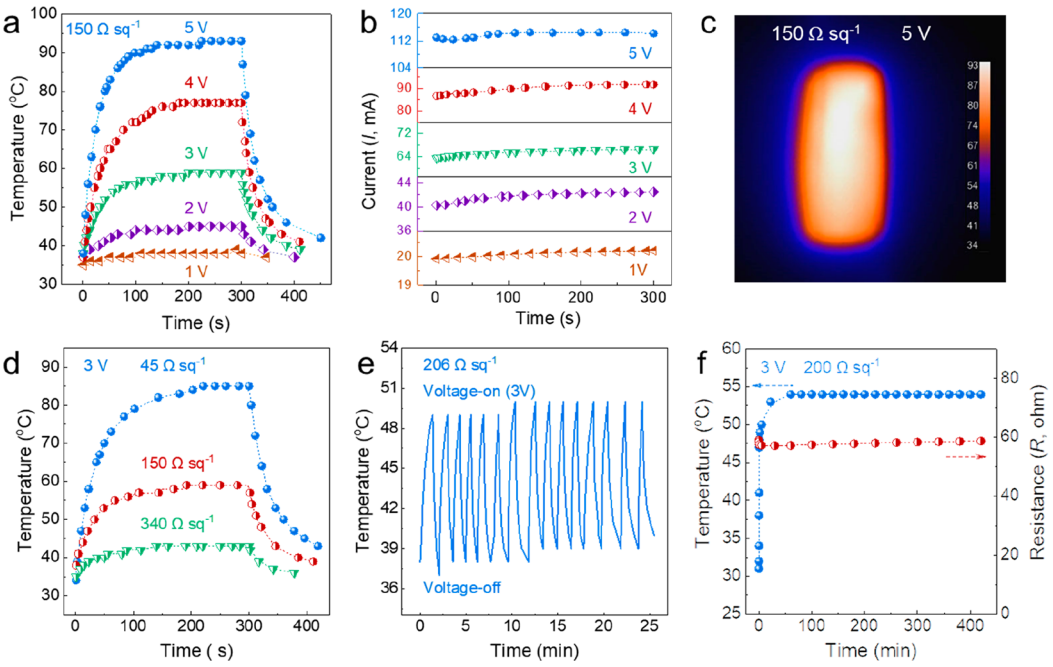

Figure 5. (a–c) thermal response of the transparent film (T = 87%, 150 Ω sq^{-1}), including the temperature response (a), current response (b) at different onset voltage, and (c) infrared radiation image at 5 V. (d) The time-varying surface temperature of the transparent film with different R_s at 3 V. (e) Thermal response of repeated on–off at an applied voltage of 3 V. (f) Temperature and resistance change in the course of continuous operation for 7 h.

Impressively, the maximum DC conductivity of the transparent $Ti_3C_2T_x$ film reaches 19 325 S cm^{-1}; even the lowest value (9780 S cm^{-1}) is quite similar to the reported best DC conductivity (9880 S cm^{-1})[7] for $Ti_3C_2T_x$ TCEs (Figure S10b,c). Importantly, these films are free from percolation problems, as when thinning down the films no precipitous conductivity decline is observed. By fitting R_s as a function of t, the average DC conductivity is derived (15 000 ± 500 S cm^{-1}, Figure 4b), significantly higher than other TCEs based on either $Ti_3C_2T_x$ or reduced graphene oxide (Figure 4c and Table S4). In addition, the inverse linear relationship between R_s and t also indicates that our MXene TCEs possess a bulk-like conductivity.[50] Using PET substrates, the TCEs (T = 74%) demonstrated an increase in resistivity ΔR% of only 3% after 10 000 bending cycles at 180° (Figure 4d). Notably, the value is substantially lower than that of previously reported $Ti_3C_2T_x$ TCEs on a PET substrate (increasing 20%, 1000 cycles).[32] Figure 4e showcases the ambient stability (R_s as a function of time) of prepared transparent films from large-sized and small-sized flakes, respectively. Obviously, the TCEs from large-sized flakes possess lower initial resistance and stronger ability to resist oxidation, and R_s increased from ∼73 to ∼143 Ω sq^{-1} after 28 days under ambient conditions. Following heat treatment (180 °C for 4 h) in an Ar atmosphere the values dropped down again to ∼108 Ω sq^{-1}. This indicates that the increased resistance of TCEs under ambient conditions is caused by the synergistic effect of adsorption of water molecules and partial oxidation. As a result, we can conclude that moisture is an important factor affecting the R_s of the film under ambient atmosphere, and it is related to the initial resistance of the films.

Joule-Heating Performance of Transparent $Ti_3C_2T_x$ Films. The excellent electrical conductivity enables tremendous potential of $Ti_3C_2T_x$ TCEs in the field of thermoelectrics, such as healthcare and thermotherapy, through Joule heating.[11,24] Fabricating transparent Joule heaters is of high significance, as it allows the direct visualizing of skin under the TCEs. Nevertheless, preparing high-performance Joule heaters with quick response time and low onset voltage is still quite challenging. This is because highly transparent films typically encounter high sheet resistance, leading to a high onset voltage to reach the desired temperature. Here the excellent optoelectronic properties in the as-fabricated MXene TCEs may suggest their promising application for advanced Joule heaters. Several transparent $Ti_3C_2T_x$ TCEs with R_s from 45 Ω sq^{-1} (∼T = 67%) to 340 Ω sq^{-1} (∼T = 93%) were selected for Joule-heating analysis. As shown in Figure 5a, the temperature–time curves showcase the saturation temperature of the film with R_s = 150 Ω sq^{-1} (∼T = 87%) gradually increasing from 39, to 45, 59, 77, and 93 °C as the applied voltage is increased from 1 V, to 2, 3, 4, and 5 V, respectively. According to Joule's law, $Q = \frac{V^2}{R}t$, where Q is the heat generated by the Joule effect, V is the applied voltage, R is the resistance of the electrode, and t is the time. Obviously, the heat generated is related to the applied voltage and resistance. Here, the response time from room temperature to near saturation temperature is about 86 s at 5 V, which is significantly lower than that of opaque $Ti_3C_2T_x$ coating commercial cellulose fabric (16 s@100 °C, 6 V),[24] Ag micromesh/$Ti_3C_2T_x$ (28 s@99 °C, T = 80%, 1.2 V),[51] and PVDF-AgNW/$Ti_3C_2T_x$ (25 s@77 °C, 2.5 V),[52] depending on the resistance of the electrode. However, for highly transparent electrodes, this is desirable and acceptable. After applying a voltage to the $Ti_3C_2T_x$ electrodes, the corresponding current values gradually increase to a constant value (Figure 5b), indicating that applying a voltage improves the conductivity and could be explained as the removal of surface species on the $Ti_3C_2T_x$ TCEs.[53] The infrared radiation (IR) image of R_s = 150 Ω sq^{-1} at 5 V is

https://doi.org/10.1021/acsnano.2c11180
ACS Nano 2023, 17, 3737–3749

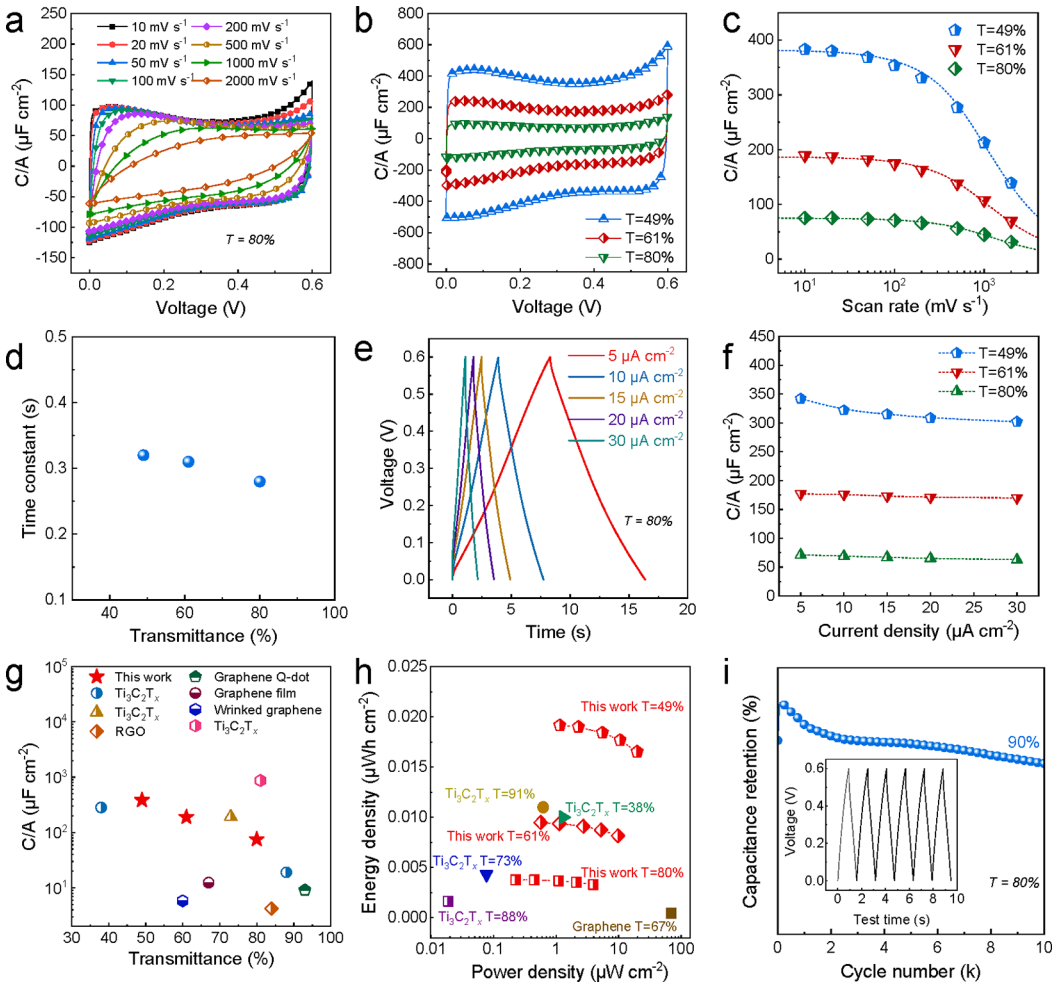

Figure 6. Electrochemical characterization of a transparent $Ti_3C_2T_x$ MSC. (a) Normalized CV curves at various scan rates of the MSC device with T = 80%. (b) CV curves with different transparency at 10 mV s^{-1}. (c) Measured areal capacitance obtained from CV curves. The dashed lines represent the capacitance fitting value according to eq 5. (d) The obtained time constant (Figure 6c), versus transmittance. (e) GCD curves at different current densities of devices, T = 80%. (f) Measured areal capacitance obtained from GCD curves of various transparency symmetric micro-supercapacitors. (g) Areal capacitance versus transmittance and comparison to other transparent supercapacitors. Detailed values are presented in Table S5. (h) Ragone plots of symmetric supercapacitors using different transparent electrodes and comparison to other transparent supercapacitors. Detailed values are presented in Table S6. (i) Long-term cycling of the transparent micro-supercapacitor (T = 80%). Note, the transmittance of the electrode before laser engraving is defined as the transmittance of the MSC, while the transmittance of the interdigitated MSC after laser engraving is much higher than that of the electrode before engraving; furthermore the transmittance of the MSC depends on the interdigitated finger gap of the MSC.

shown in Figure 5c, indicating the $Ti_3C_2T_x$ thin film possesses good thermal uniformity.

The sheet resistance of the transparent electrode is a crucial factor affecting the surface saturation temperature; low sheet resistance can convert more heat at a given applied voltage. We investigated the electrothermal properties of $Ti_3C_2T_x$ films with different sheet resistance. For the T = 67% film with R_s = 45 Ω sq^{-1}, the saturated temperature reaches 86 and 115 °C under the applied voltage of 3 V (Figure 5d) and 4 V (Figure S11a,b,c), while the corresponding current values decrease above 86 °C, indicating continuous deterioration of service life, despite the constant temperature detected by IR thermometer. This phenomenon is not observed in the transparent electrode with R_s = 150 Ω sq^{-1} (no attenuation), which is mainly due to the fact that the lower sheet resistance electrode possesses a higher current value (45 Ω sq^{-1}, ~300 mA, 4 V) than the high sheet resistance electrode (150 Ω sq^{-1}, 113 mA, 5 V). Although the electrode of 150 Ω sq^{-1} reached 93 °C at 5 V, it can still maintain a constant current within a certain time frame. Consequently, it is necessary to balance the relationship between applied voltage, response saturation temperature, and lifespan. For the highly transparent film (R_s = 340 Ω sq^{-1}, T = 93%), an onset voltage results in a saturated temperature of 43 °C (Figure 5d) and 62 °C (Figure S12d,e,f) under 3 and 5 V, respectively. Moreover, the Joule-heating effect of the $Ti_3C_2T_x$ thin film (206 Ω sq^{-1}) demonstrated excellent cyclic on−off thermal response at the applied voltage of 3 V, as shown in Figure 5e. The saturation temperature can be maintained at 50 ± 1 °C during 15 cycles without a decline in thermal response time. The Joule heater durability of the MXene TCE (200 Ω sq^{-1}) was evaluated by measuring the temperature changes with time at 3 V, as shown in Figure 5f. After 7 h of continuous operation, the maximum temperature remains constant with negligible resistance changes, demonstrating the excellent durability of our MXene TCE as transparent Joule heater.

Electrochemical Performance of Transparent $Ti_3C_2T_x$ Films. Finally, we investigated the electrochemical charge storage properties of symmetric micro-supercapacitors (MSCs,

https://doi.org/10.1021/acsnano.2c11180
ACS Nano 2023, 17, 3737−3749

interdigitated finger gap ~260 μm, Figure S12) based on $Ti_3C_2T_x$ TCEs. The normalized cyclic voltammograms (CVs) of MSC were studied from 10 mV s^{-1} to 2000 mV s^{-1} as shown in Figure 6a and Figure S13. The MSC with a device transmittance of T = 80% exhibits a quasi-rectangular shape below 500 mV s^{-1} and favorable capacitance even at 2000 mV s^{-1} (maintaining 42% of initial capacitance at 10 mV s^{-1}), indicating excellent rate performance. A quick CV comparison of MSCs with T = 80%, 61%, and 49% at 10 mV s^{-1} indicates that thicker films lead to higher capacitances, as seen in the gradually enlarged encircled area under the CV curves (Figure 6b). This electrochemical behavior is similar to that of opaque $Ti_3C_2T_x$ based supercapacitors,[20,21] indicating that our films have a good application prospect in the field of transparent energy storage devices. However, the thicker film showcases a sluggish time response upon voltage reversal at 100 mV s^{-1} compared to 10 mV s^{-1}, coupled with the broad peak position (0−0.15 V) shifting to higher voltage (Figure S14). The areal capacitances of $Ti_3C_2T_x$ at different scan rates were calculated from CV curves (Figure 6c) and were fitted based on eq 5,[15]

$$C = C_0\left[1 - \frac{\nu\tau}{\Delta V}(1 - e^{-\Delta V/\nu\tau})\right] \quad (5)$$

where $\tau = R_{ESR}C$ is the time constant, ν is the scan rate, ΔV is the voltage window (0.6 V), and C_0 is the intrinsic, rate-independent areal capacitance (no electronic and/or ionic transport limitations during charge−discharge). The time constant extracted from the fits is used to characterize the migration kinetics of ions; a smaller time constant indicates faster ion migration. The T = 80% MSC exhibits 75.2 μF cm^{-2} at 10 mV s^{-1} from the experimental measurement; the value is slightly higher than that of graphene transparent films (T = 67%@12.4 μF cm^{-2}, T = 84%@4.2 μF cm^{-2}).[54,55] However, it is substantially lower than the values for the small-size $Ti_3C_2T_x$-based MSC at similar transparency (T = 81%@870 μF cm^{-2}).[7] The T = 61% and T = 49% MSCs exhibit 189.5 and 383.2 μF cm^{-2} at 10 mV s^{-1}, respectively. This highlights the importance of flake size engineering when the TCEs are used for transparent energy storage devices. The lower capacitance at higher rates for thicker film-based MSCs can be explained with the larger time constant (Figure 6d). The galvanostatic charge−discharge (GCD) curves of MSCs are symmetric and triangular, indicating typical capacitive-like behavior (Figure 6e). The capacitance values derived from GCD curves are shown in Figure 6f. In addition, as the current density increases from 5 μA cm^{-2} to 30 μA cm^{-2}, a high capacitance of 88% was achieved, suggesting very good rate handling properties in our transparent solid-state MXene MSCs. Figure 6g and Table S5 compare the areal capacitance of this work with other reported transparent MSC devices. The energy density and power density of $Ti_3C_2T_x$ MSC with different transmittances were further calculated and compared with previous transparent MSC devices (Figure 6h, Table S6). The maximum energy density of our MXene MSC (T = 80%) reaches 0.004 μWh cm^{-2} (at a power density of 0.23 μW cm^{-2}), which has greatly outperformed that of other MSCs, *i.e.*, graphene (0.00047 μWh cm^{-2}, T = 67%).[55] The transparent MXene MSC also showcases an outstanding cycling performance, retaining 90% of the initial capacitance after 10 000 cycles (Figure 6i). These outstanding charge storage properties indicate the promising future of MXene MSCs for scalable fabrication of solid-state, advanced transparent MSCs to power microelectronics.

CONCLUSION

In summary, we have fabricated high-performance $Ti_3C_2T_x$ TCEs with compact microstructures, well orientated by room-temperature blade-shearing of the high-quality (predominantly single-layer, clean surface, narrow size distribution) additive-free MXene aqueous ink. The ultralarge, high-aspect-ratio flakes are forced to align, forming well-stacked, interconnected conductive paths without notorious percolation issues. Consequently, blade-coated MXene films achieved ultrahigh DC conductivity up to 19 325 S cm^{-1} at transmittances of 83.4% (≈6.7 nm). Such advanced optoelectronic properties ensure an excellent Joule-heating effect (thermal homogeneousness, durability, low onset voltage) and high rate response in transparent Joule heaters and transparent MSCs, respectively. The excellent optoelectric, electrothermal, and electrochemical properties suggest potential applications in flexible, transparent electronic devices. It is expected that the optoelectronic performance can be further improved by further boosting the flake sizes, optimizing the synthesis of MXene, regulating the surface chemistry, or/and the doping of pure $Ti_3C_2T_x$, to name just a few.

METHODS

Purification and Size Selection of Ti_3AlC_2 MAX Phase. The as-received Ti_3AlC_2 particles (10 g) were stirred continuously in 9 M HCl (35 mL) for 12 h and then dried for future use. The large-sized MAX phase was obtained following a modified version of a previously reported method.[34] The purified MAX phase was dispersed in 50 mL of deionized water (centrifuge tube, height = 10 cm) and shaken evenly. After the dispersion was kept stationary for 82 s, the upper suspension was removed to separate the MAX phase particles larger than 25 μm, repeated three times. The large-size MAX sediment was collected and dried for further use. The standing time for the dispersion was selected based on the terminal velocity (υ, m s^{-1}) according to eq 6:

$$\upsilon = \frac{2(\rho_p - \rho_f)gR^2}{9\mu} \quad (6)$$

where g is the gravitational acceleration (m s^{-2}), R is the radius of the spherical particle, ρ_p is the mass density of the Ti_3AlC_2 MAX phase particles (~4.2 × 10^3 kg m^{-3}), ρ_f is the mass density of water (10^3 kg m^{-3}), and μ is the dynamic viscosity (Pa s or kg m^{-1} s^{-1}) of water (8.90 × 10^{-4} Pa s at ~25 °C).

Synthesis of Delaminated Large-Sized $Ti_3C_2T_x$. The large-sized $Ti_3C_2T_x$ was synthesized using a modified minimally intensive layer delamination method (MILD). Compared to the small-sized Ti_3AlC_2 MAX phase, the LiF/MAX ratio and etch time were optimized. Specifically, 2.4 g of LiF was slowly added into 9 M HCl (30 mL) and stirred continuously for 10 min in an oil bath of 50 °C. In the following 0.75 g of MAX phase was added to the above-mentioned solution in batches. After 48 h, the etched sediment was washed with deionized water and centrifuged at 1500 rcf for 5 min, and the supernatant was decanted. The process was repeated several times until the supernatant appeared dark-green and the pH value of the supernatant approached ~6. Then, 40 mL of deionized water was added to the precipitate under manual shaking until the precipitate is completely redispersed (the suspension is centrifuged at 1500 rcf for 5 min, redispersed by manual shaking, without decanting the upper suspension, and repeated several times to improve the yield of $Ti_3C_2T_x$ flakes). Furthermore, the samples were placed on a vortex machine and shaken for 30 min to improve the yield. After that, the suspension was centrifuged at 1500 rcf for 30 min. The upper black-green suspension was collected and labeled as a $Ti_3C_2T_x$ colloidal solution with wider size distribution. Further, the colloidal solution was centrifuged at 3000 rcf for 15 min (the suspension contains relatively small nanosheets, the sediment was redispersed with

https://doi.org/10.1021/acsnano.2c11180
ACS Nano 2023, 17, 3737−3749

deionized water by vigorous shaking), repeated twice. The sediment was collected, which now contains predominantly ultralarge-sized single-layer $Ti_3C_2T_x$ flakes and labeled as ultralarge-sized $Ti_3C_2T_x$ flakes and placed in a refrigerator at 4 °C. Finally, the precipitate was diluted to a specific concentration for blade-coating. The concentration of the delaminated $Ti_3C_2T_x$ was determined by vacuum filtration with a Celgard membrane (Celgard 3501, PP coated, USA) and a known volume of the $Ti_3C_2T_x$ aqueous solution.

Synthesis of Small-Sized $Ti_3C_2T_x$. We prepared small-sized $Ti_3C_2T_x$ flakes by ultrasonification. Specifically, 0.8 g of LiF was slowly added into 9 M HCl (10 mL) and stirred continuously for 10 min in an oil bath of 35 °C. In the following 0.5 g of Ti_3AlC_2 MAX phase was added to the above solution in batches. After 24 h, the etched sediment was washed with deionized water and centrifuged at 1500 rcf for 5 min, and the supernatant was decanted. The process was repeated several times until the supernatant appeared dark-green and the pH value of the supernatant approached ~6. Then, 100 mL of deionized water was added to the precipitate, and manual shaking was applied until the precipitates were completely redispersed. The suspension was continuously sonicated under an Ar atmosphere (after being degassed for 10 min) in an ice bath for 30 min, 35 kHz. The dispersion was centrifuged at 1500 rcf for 30 min, and the upper suspension was collected and labeled as small-sized $Ti_3C_2T_x$ flakes.

Production of Transparent, Conductive Thin Films. The transparent, conductive films were fabricated by blade-coating on glass and PET substrates in a class 5 clean-room. First, glass substrates were cleaned with a soap solution, ethanol, and deionized water, sequentially. After that, all the glass substrates and PET were plasma cleaned (Diener Plasma surface technology) for 2 min under vacuum (0.47 mbar), to obtain a hydrophilic surface. The conductive $Ti_3C_2T_x$ films with various transparency were fabricated by adjusting the blade height and the concentration of the $Ti_3C_2T_x$ solution. The films of transmittance >80% were prepared using a 2−10 mg mL^{-1} dispersion of large-sized $Ti_3C_2T_x$ flakes at gap sizes of 15 μm, and the blade moving speed was controlled at 30−40 mm s^{-1}. The films of transmittance of 40−80% were prepared using approximately 10−30 mg mL^{-1} dispersions at a gap height of 20 μm. The overconcentration of $Ti_3C_2T_x$ solution is not conducive for the transparent and homogeneous films. The transparent films were transferred to a glovebox and annealed at 180 °C for 4 h (glass substrate) to eliminate the trapped water between the flakes. All samples were stored in the glovebox for future use.

Morphology Characterization. SEM and TEM imaging of $Ti_3C_2T_x$ flakes were performed on a NanoSEM 230 and a JEOL 2200 FS using an accelerating voltage of 200 kV. XRD patterns of $Ti_3C_2T_x$ films were obtained using an X'Pert Pro with Cu Kα radiation (λ = 0.15406 nm). Atomic force microscopy measurements were performed on a Bruker ICON3 in the peak force scanasyst mode. Raman spectra of transparent films were measured using a Renishaw Raman microscope (633 nm).

GISAXS spectra of thin films were collected on a Bruker NanoStar (Bruker AXS GmbH, Karlsruhe, Germany) at the Center for X-ray Analytics at EMPA St. Gallen. The instrument was equipped with a pinhole collimation system, allowing a beam size at a sample position of about 400 μm in diameter. X-ray generation was sustained with a microfocused X-ray Cu source (wavelength Cu Kα = 1.5406 Å), and scattering patterns were recorded on a 2D MikroGap technology-based detector (VÅNTEC-2000 2D with 2048 × 2048 pixels and 68 × 68 μm pixel size) along with a standard beam stop. In the SAXS experimental configuration, the sample to detector distance was set at 27 cm and was further calibrated with a silver behenate powder standard, resulting in a scattering vector modulus q covering a range between 0.11 and 10.34 nm^{-1}. To limit air scattering, the scattering patterns were recorded at room temperature under moderate vacuum conditions (10^{-2} mbar). Scattering of each sample was recorded over an integration time of 100 s, acquiring a good signal-to-noise ratio data set. Intensity data have been flat field, efficiency and spatially corrected, accounting for variations in the detector's pixel-to-pixel sensitivity and geometry. Azimuthal profiles of (002) were recorded based on peak maxima $q_z \approx 6.2$ nm^{-1} and fitted with a Lorentzian distribution curve. Herman's orientation factor (f) calculation was used to describe the degree of orientation of the MXene flakes relative to the surface of the glass using the following eqs 7 and 8:[34,56]

$$f = \frac{3\cdot(\cos^2\text{Ø})}{2} \tag{7}$$

where $\langle\cos^2\text{Ø}\rangle$ is the mean-square cosine calculated from the scattered intensity $I(\text{Ø})$ integrated over the azimuthal angle following

$$(\cos^2\text{Ø}) = \frac{\int_0^{\pi/2} \mathrm{I}(\text{Ø})\cdot \sin \text{Ø}\cdot\cos^2\text{Ø}\cdot \mathrm{d}\text{Ø}}{\int_0^{\pi/2} \mathrm{I}(\text{Ø})\cdot \sin \text{Ø}\cdot \mathrm{d}\text{Ø}} \tag{8}$$

The Herman's orientation factor (f) values range from $-0.5 \le f \le 1.0$. If f is equal to −0.5, the orientation of flakes is perpendicular to the reference, *i.e.*, flow, direction (φ = 90°), if f is equal to 1, the orientation is parallel to the reference direction (φ = 0°), and if f is equal to 0, a random orientation is present.

Optoelectronic Property Measurements. The transmittance of the transparent electrode was measured by a UV−vis spectrophotometer (Varian Cary 50) in the wavelength range 350−800 nm. The transmittance at 550 nm is labeled as the transmittance of the films. The sheet resistance (R_s) was tested with a four-point probe (Jandel, model RM3-AR), and the values were obtained by averaging 10 different regions for each sample. The thickness measurement of the low-transparency conductive films was performed by a programmable surface profiler (DEKTAK 6M), and the values were obtained by averaging in five different regions for each sample.

Joule-Heating Characterization. The transparent heaters were powered with a DC voltage source (Keithley 2400). Temperature and thermal images were recorded by an IR camera (Seekthermal). The sample size was about 0.5 × 1.5 cm, and the height between the sample and the IR camera was about 7 cm.

Electrochemical Characterization. PVA/H2SO4 hydrogel was obtained based on our previously reported method.[7] Typically, 1 g of poly(vinyl alcohol) (PVA) powder was added to 10 mL of deionized water. Then the suspension was stirred vigorously at 85 °C until the solution became clear. After cooling down, 3 g of concentrated H_2SO_4 (97 wt.%) was added to the above solution, followed by another 1 h of vigorous stirring at room temperature. The transparent films were blade-coated onto a glass substrate. Consecutively the film was patterned by laser scribing (TruMark Station 5000) to prepare micro-supercapacitors. The laser scribing pattern was designed by TRUMPF software (interdigitated finger gap ~260 μm). The electrochemical performance of the prepared micro-supercapacitors was evaluated by CV and GCD on a VMP3 potentiostat (BioLogic, France). The CVs of transparent supercapacitors were performed at 10−2000 mV s^{-1}, and the GCD was performed at 2−30 μA cm^{-2} in a voltage window of 0.6 V. The area capacitance of the supercapacitor device was calculated from the third cycle of each CV test by eq 9:

$$C = \frac{\int_0^{0.6} j\mathrm{d}V}{A\Delta V\upsilon} \tag{9}$$

where C is the area capacitance of supercapacitors (μA cm^{-2}), j is the current (mA), ΔV is the voltage window (0.6 V), A is the geometric area of the MSC (0.38 cm^2), and υ is the scan rate (mV s^{-1}). We also calculated the area capacitance of the supercapacitor device through the third cycle of each GCD curve according to eq 10:

$$C = \frac{j\Delta t}{A\Delta V} \tag{10}$$

where ΔV is the effective voltage window excluding the IR drop. Δt is the discharge time.

ASSOCIATED CONTENT

Supporting Information

The Supporting Information is available free of charge at https://pubs.acs.org/doi/10.1021/acsnano.2c11180.

https://doi.org/10.1021/acsnano.2c11180
ACS Nano 2023, 17, 3737−3749

Schematic illustration of the synthesis process, XRD spectra of MXene films, SEM and TEM images of MXene flakes, digital photography of MXene films on glass and PET, SEM images from previously published works on transparent MXene films, cross-sectional SEM image and GISAXS detector image of MXene films, methodology to extract average film thickness of ultrathin films, electrochemical characterization of films, relationship between $Ti_3C_2T_x$ films thickness and optoelectronic properties, electrothermal properties of $Ti_3C_2T_x$ films (PDF)

AUTHOR INFORMATION

Corresponding Authors

Di Zhou − *Key Laboratory of Multifunctional Materials and Structures, Ministry of Education, School of Electronic Science and Engineering, Xi'an Jiaotong University, Xi'an 710049 Shaanxi, China*; Email: zhoudi1220@xjtu.edu.cn

Jakob Heier − *Laboratory for Functional Polymers, Empa, Swiss Federal Laboratories for Materials Science and Technology, CH-8600 Dübendorf, Switzerland*; orcid.org/0000-0003-2189-3162; Email: Jakob.Heier@empa.ch

Chuanfang Zhang − *College of Materials Science & Engineering, Sichuan University, Chengdu 610065 Sichuan, China*; Email: chuanfang.zhang@scu.edu.cn

Authors

Tiezhu Guo − *Key Laboratory of Multifunctional Materials and Structures, Ministry of Education, School of Electronic Science and Engineering, Xi'an Jiaotong University, Xi'an 710049 Shaanxi, China; Laboratory for Functional Polymers, Empa, Swiss Federal Laboratories for Materials Science and Technology, CH-8600 Dübendorf, Switzerland*

Shungui Deng − *Laboratory for Functional Polymers, Empa, Swiss Federal Laboratories for Materials Science and Technology, CH-8600 Dübendorf, Switzerland; Institute of Materials Science and Engineering, Ecole Polytechnique Federale de Lausanne (EPFL), CH-1015 Lausanne, Switzerland*

Mohammad Jafarpour − *Laboratory for Functional Polymers, Empa, Swiss Federal Laboratories for Materials Science and Technology, CH-8600 Dübendorf, Switzerland; Institute of Materials Science and Engineering, Ecole Polytechnique Federale de Lausanne (EPFL), CH-1015 Lausanne, Switzerland*

Jonathan Avaro − *Center for X-ray Analytics and Biomimetic Membranes and Textile, Empa, Swiss Federal Laboratories for Materials Science and Technology, CH-9014 St. Gallen, Switzerland*; orcid.org/0000-0001-6596-3228

Antonia Neels − *Center for X-ray Analytics, Empa, Swiss Federal Laboratories for Materials Science and Technology, CH-8600 Dübendorf, Switzerland; Department of Chemistry, University of Fribourg, CH-1700 Fribourg, Switzerland*; orcid.org/0000-0001-5752-2852

Complete contact information is available at: https://pubs.acs.org/10.1021/acsnano.2c11180

Notes

The authors declare no competing financial interest.

ACKNOWLEDGMENTS

C.Z. designed the project and experiments. T.G. performed materials synthesis and characterization experiments. T.G. wrote the original manuscript. D.Z. commented on the manuscript and supported the research of T.G. S.D. and J.H. helped with the data analysis, partial characterization experiments, and critical comments for this manuscript. All the authors reviewed and commented on the manuscript. M.J. provided the film's Raman and TEM measurements. J.A. and A.N. provided the film's GISAXS characterization and analysis. We thank Robin Bucher (Empa) for FIB-SEM. The work was supported by the International Cooperation Project of Shaanxi Province (2021KWZ-10), the Fundamental Research Funds for the Central University, the 111 Project of China (B14040), and and China Scholarship Council (202106280247). Funding from the ETH board (SFA-AM project SCALAR) is acknowledged.

REFERENCES

(1) De, S.; Coleman, J. N. Are there fundamental limitations on the sheet resistance and transmittance of thin graphene films? *ACS Nano* **2010**, *4*, 2713−2720.

(2) Hecht, D. S.; Hu, L.; Irvin, G. Emerging transparent electrodes based on thin films of carbon nanotubes, graphene, and metallic nanostructures. *Adv. Mater.* **2011**, *23*, 1482−1513.

(3) Zhou, B.; Su, M.; Yang, D.; Han, G.; Feng, Y.; Wang, B.; Ma, J.; Ma, J.; Liu, C.; Shen, C. Flexible MXene/silver nanowire-based transparent conductive film with electromagnetic interference shielding and electro-photo-thermal performance. *ACS Appl. Mater. Interfaces* **2020**, *12*, 40859−40869.

(4) Zhang, C.; Nicolosi, V. Graphene and MXene-based transparent conductive electrodes and supercapacitors. *Energy Storage Mater.* **2019**, *16*, 102−125.

(5) Vosgueritchian, M.; Lipomi, D. J.; Bao, Z. Highly conductive and transparent PEDOT:PSS films with a fluorosurfactant for stretchable and flexible transparent electrodes. *Adv. Funct. Mater.* **2012**, *22*, 421−428.

(6) Zhang, C.; Higgins, T. M.; Park, S. H.; O'Brien, S. E.; Long, D.; Coleman, J. N.; Nicolosi, V. Highly flexible and transparent solid-state supercapacitors based on RuO_2/PEDOT:PSS conductive ultrathin films. *Nano Energy* **2016**, *28*, 495−505.

(7) Zhang, C. J.; Anasori, B.; Seral-Ascaso, A.; Park, S. H.; McEvoy, N.; Shmeliov, A.; Duesberg, G. S.; Coleman, J. N.; Gogotsi, Y.; Nicolosi, V. Transparent, flexible, and conductive 2D titanium carbide (MXene) films with high volumetric capacitance. *Adv. Mater.* **2017**, *29*, 1702678.

(8) Wang, T.; Wang, Y. Z.; Jing, L. C.; Zhu, Q.; Ethiraj, A. S.; Geng, W.; Tian, Y.; Zhu, Z.; Meng, Z.; Geng, H. Z. Novel biodegradable and ultra-flexible transparent conductive film for green light OLED devices. *Carbon* **2021**, *172*, 379−389.

(9) Zhu, J.; Han, D.; Wu, X.; Ting, J.; Du, S.; Arias, A. C. Highly flexible transparent micromesh electrodes via blade-coated polymer networks for organic light-emitting diodes. *ACS Appl. Mater. Interfaces* **2020**, *12*, 31687−31695.

(10) Tang, H.; Feng, H.; Wang, H.; Wan, X.; Liang, J.; Chen, Y. Highly conducting MXene-silver nanowire transparent electrodes for flexible organic solar cells. *ACS Appl. Mater. Interfaces* **2019**, *11*, 25330−25337.

(11) Wang, Q.; Sheng, H.; Lv, Y.; Liang, J.; Liu, Y.; Li, N.; Xie, E.; Su, Q.; Ershad, F.; Lan, W.; Wang, J.; Yu, C. A skin-mountable hyperthermia patch based on metal nanofiber network with high transparency and low resistivity toward subcutaneous tumor treatment. *Adv. Funct. Mater.* **2022**, *32*, 2111228.

(12) He, X.; Shen, G.; Xu, R.; Yang, W.; Zhang, C.; Liu, Z.; Chen, B.; Liu, J.; Song, M. Hexagonal and square patterned silver nanowires/PEDOT:PSS composite grids by screen printing for uniformly transparent heaters. *Polymers (Basel)* **2019**, *11*, 468.

(13) Liu, J.; Zhang, Y.; Cheng, W.; Lei, S.; Song, L.; Wang, B.; Hu, Y. Anti-fogging, frost-resistant transparent and flexible silver nanowire-$Ti_3C_2T_x$ MXene based composite films for excellent electromagnetic interference shielding ability. *J. Colloid Interface Sci.* **2022**, *608*, 2493−2504.
(14) Wang, Z.; Wang, P.; Cao, W.; Sun, C.; Song, Z.; Ji, D.; Yang, L.; Han, J.; Zhu, J. Robust, transparent, and conductive agnw/MXene composite polyurethane self-healing film for electromagnetic interference shielding. *J. Mater. Chem. C* **2022**, *10*, 17066−17074.
(15) Higgins, T. M.; Coleman, J. N. Avoiding resistance limitations in high-performance transparent supercapacitor electrodes based on large-area, high-conductivity PEDOT:PSS films. *ACS Appl. Mater. Interfaces* **2015**, *7*, 16495−16506.
(16) Nair, R. R.; Blake, P.; Grigorenko, A. N.; Novoselov, K. S.; Booth, T. J.; Stauber, T.; Peres, N. M.; Geim, A. K. Fine structure constant defines visual transparency of graphene. *Science* **2008**, *320*, 1308.
(17) Mak, K. F.; Sfeir, M. Y.; Wu, Y.; Lui, C. H.; Misewich, J. A.; Heinz, T. F. Measurement of the optical conductivity of graphene. *Phys. Rev. Lett.* **2008**, *101*, 196405.
(18) VahidMohammadi, A.; Rosen, J.; Gogotsi, Y. The world of two-dimensional carbides and nitrides (MXenes). *Science* **2021**, *372*, 1165.
(19) Gogotsi, Y.; Anasori, B. The rise of MXenes. *ACS Nano* **2019**, *13*, 8491−8494.
(20) Guo, T.; Fu, M.; Zhou, D.; Pang, L.; Su, J.; Lin, H.; Yao, X.; Sombra, A. S. B. Flexible $Ti_3C_2T_x$/graphene films with large-sized flakes for supercapacitors. *Small Struct* **2021**, *2*, 2100015.
(21) Guo, T.; Zhou, D.; Pang, L.; Darwish, M. A.; Shi, Z. Sandwich-type macroporous $Ti_3C_2T_x$ MXene frameworks for supercapacitor electrode. *Scripta Mater.* **2022**, *213*, 114590.
(22) Chen, W.; Liu, L. X.; Zhang, H. B.; Yu, Z. Z. Flexible, transparent, and conductive $Ti_3C_2T_x$ MXene-silver nanowire films with smart acoustic sensitivity for high-performance electromagnetic interference shielding. *ACS Nano* **2020**, *14*, 16643−16653.
(23) Zhao, M. Q.; Xie, X.; Ren, C. E.; Makaryan, T.; Anasori, B.; Wang, G.; Gogotsi, Y. Hollow MXene spheres and 3D macroporous MXene frameworks for na-ion storage. *Adv. Mater.* **2017**, *29*, 1702410.
(24) Zhao, X.; Wang, L. Y.; Tang, C. Y.; Zha, X. J.; Liu, Y.; Su, B. H.; Ke, K.; Bao, R. Y.; Yang, M. B.; Yang, W. Smart $Ti_3C_2T_x$ MXene fabric with fast humidity response and joule heating for healthcare and medical therapy applications. *ACS Nano* **2020**, *14*, 8793−8805.
(25) Guo, T.; Zhou, D.; Zhang, C. Perspectives on electrochemical nitrogen fixation catalyzed by two-dimensional MXenes. *Mater. Rep. Energy* **2022**, *2*, 100076.
(26) Dillon, A. D.; Ghidiu, M. J.; Krick, A. L.; Griggs, J.; May, S. J.; Gogotsi, Y.; Barsoum, M. W.; Fafarman, A. T. Highly conductive optical quality solution-processed films of 2D titanium carbide. *Adv. Funct. Mater.* **2016**, *26*, 4162−4168.
(27) Ying, G.; Kota, S.; Dillon, A. D.; Fafarman, A. T.; Barsoum, M. W. Conductive transparent V_2CT_x (MXene) films. *FlatChem.* **2018**, *8*, 25−30.
(28) Ebrahimi, M.; Mei, C. T. Optoelectronic properties of $Ti_3C_2T_x$ MXene transparent conductive electrodes: Microwave synthesis of parent max phase. *Ceram. Int.* **2020**, *46*, 28114−28119.
(29) Wen, D.; Wang, X.; Liu, L.; Hu, C.; Sun, C.; Wu, Y.; Zhao, Y.; Zhang, J.; Liu, X.; Ying, G. Inkjet printing transparent and conductive MXene ($Ti_3C_2T_x$) films: A strategy for flexible energy storage devices. *ACS Appl. Mater. Interfaces* **2021**, *13*, 17766−17780.
(30) Hantanasirisakul, K.; Zhao, M. Q.; Urbankowski, P.; Halim, J.; Anasori, B.; Kota, S.; Ren, C. E.; Barsoum, M. W.; Gogotsi, Y. Fabrication of $Ti_3C_2T_x$ MXene transparent thin films with tunable optoelectronic properties. *Adv. Electron. Mater.* **2016**, *2*, 1600050.
(31) Huang, L.; Lin, Y.; Zeng, W.; Xu, C.; Chen, Z.; Wang, Q.; Zhou, H.; Yu, Q.; Zhao, B.; Ruan, L.; Wang, S. Highly transparent and flexible zn-$Ti_3C_2T_x$ MXene hybrid capacitors. *Langmuir* **2022**, *38*, 5968−5976.
(32) Kumar, S.; Kang, D.; Nguyen, V. H.; Nasir, N.; Hong, H.; Kim, M.; Nguyen, D. C.; Lee, Y. J.; Lee, N.; Seo, Y. Application of titanium-carbide MXene-based transparent conducting electrodes in flexible smart windows. *ACS Appl. Mater. Interfaces* **2021**, *13*, 40976−40985.
(33) Ying, G.; Dillon, A. D.; Fafarman, A. T.; Barsoum, M. W. Transparent, conductive solution processed spincast 2D Ti_2CT_x (MXene) films. *Mater.Res. Lett.* **2017**, *5*, 391−398.
(34) Zhang, J.; Kong, N.; Uzun, S.; Levitt, A.; Seyedin, S.; Lynch, P. A.; Qin, S.; Han, M.; Yang, W.; Liu, J.; Wang, X.; Gogotsi, Y.; Razal, J. M. Scalable manufacturing of free-standing, strong $Ti_3C_2T_x$ MXene films with outstanding conductivity. *Adv. Mater.* **2020**, *32*, No. e2001093.
(35) Wan, S. J.; Li, X.; Chen, Y.; Liu, N. N.; Du, Y.; Dou, S. X.; Jiang, L.; Cheng, Q. F. High-strength scalable MXene films through bridging-induced densification. *Science* **2021**, *374*, 96.
(36) Lee, G. S.; Yun, T.; Kim, H.; Kim, I. H.; Choi, J.; Lee, S. H.; Lee, H. J.; Hwang, H. S.; Kim, J. G.; Kim, D. W.; Lee, H. M.; Koo, C. M.; Kim, S. O. Mussel inspired highly aligned $Ti_3C_2T_x$ MXene film with synergistic enhancement of mechanical strength and ambient stability. *ACS Nano* **2020**, *14*, 11722−11732.
(37) Zhang, L.; Lin, B.; Hu, B.; Xu, X.; Ma, W. Blade-cast nonfullerene organic solar cells in air with excellent morphology, efficiency, and stability. *Adv. Mater.* **2018**, *30*, No. e1800343.
(38) Ma, W.; Reinspach, J.; Zhou, Y.; Diao, Y.; McAfee, T.; Mannsfeld, S. C. B.; Bao, Z.; Ade, H. Tuning local molecular orientation-composition correlations in binary organic thin films by solution shearing. *Adv. Funct. Mater.* **2015**, *25*, 3131−3137.
(39) Abdolhosseinzadeh, S.; Jiang, X.; Zhang, H.; Qiu, J.; Zhang, C. Perspectives on solution processing of two-dimensional MXenes. *Mater. Today* **2021**, *48*, 214−240.
(40) Hantanasirisakul, K.; Chantaurai, T.; Limsukhon, A.; Chomkhuntod, P.; Poprom, P.; Sawangphruk, M. Size selection and size-dependent optoelectronic and electrochemical properties of 2D titanium carbide $Ti_3C_2T_x$ MXene. *Adv. Mater. Interfaces* **2022**, *9*, 2201457.
(41) Wang, P.; Zhang, C.; Wu, M.; Zhang, J.; Ling, X.; Yang, L. Scalable solution-processed fabrication approach for high-performance silver nanowire/MXene hybrid transparent conductive films. *Nanomaterials (Basel)* **2021**, *11*, 1360.
(42) Zhao, L.; Dong, B.; Li, S.; Zhou, L.; Lai, L.; Wang, Z.; Zhao, S.; Han, M.; Gao, K.; Lu, M.; Xie, X.; Chen, B.; Liu, Z.; Wang, X.; Zhang, H.; Li, H.; Liu, J.; Zhang, H.; Huang, X.; Huang, W. Interdiffusion reaction-assisted hybridization of two-dimensional metal-organic frameworks and $Ti_3C_2T_x$ nanosheets for electrocatalytic oxygen evolution. *ACS Nano* **2017**, *11*, 5800−5807.
(43) Zhang, C. J.; Kremer, M. P.; Seral-Ascaso, A.; Park, S. H.; McEvoy, N.; Anasori, B.; Gogotsi, Y.; Nicolosi, V. Stamping of flexible, coplanar micro-supercapacitors using MXene inks. *Adv. Funct. Mater.* **2018**, *28*, 1705506.
(44) Zeng, Z.; Wang, C.; Siqueira, G.; Han, D.; Huch, A.; Abdolhosseinzadeh, S.; Heier, J.; Nuesch, F.; Zhang, C. J.; Nystrom, G. Nanocellulose-MXene biomimetic aerogels with orientation-tunable electromagnetic interference shielding performance. *Adv. Sci.* **2020**, *7*, 2000979.
(45) Salles, P.; Quain, E.; Kurra, N.; Sarycheva, A.; Gogotsi, Y. Automated scalpel patterning of solution processed thin films for fabrication of transparent MXene microsupercapacitors. *Small* **2018**, *14*, No. e1802864.
(46) Halim, J.; Cook, K. M.; Naguib, M.; Eklund, P.; Gogotsi, Y.; Rosen, J.; Barsoum, M. W. X-ray photoelectron spectroscopy of select multi-layered transition metal carbides (MXenes). *Appl. Surf. Sci.* **2016**, *362*, 406−417.
(47) Li, R.; Ma, X.; Li, J.; Cao, J.; Gao, H.; Li, T.; Zhang, X.; Wang, L.; Zhang, Q.; Wang, G.; Hou, C.; Li, Y.; Palacios, T.; Lin, Y.; Wang, H.; Ling, X. Flexible and high-performance electrochromic devices enabled by self-assembled 2D TiO_2/MXene heterostructures. *Nat. Commun.* **2021**, *12*, 1587.
(48) Mariano, M.; Mashtalir, O.; Antonio, F. Q.; Ryu, W. H.; Deng, B.; Xia, F.; Gogotsi, Y.; Taylor, A. D. Solution-processed titanium carbide MXene films examined as highly transparent conductors. *Nanoscale* **2016**, *8*, 16371−16378.

https://doi.org/10.1021/acsnano.2c11180
ACS Nano 2023, 17, 3737−3749

(49) Halim, J.; Lukatskaya, M. R.; Cook, K. M.; Lu, J.; Smith, C. R.; Naslund, L. A.; May, S. J.; Hultman, L.; Gogotsi, Y.; Eklund, P.; Barsoum, M. W. Transparent conductive two-dimensional titanium carbide epitaxial thin films. *Chem. Mater.* **2014**, *26*, 2374−2381.
(50) De, S.; Higgins, T. M.; Lyons, P. E.; Doherty, E. M.; Nirmalraj, P. N.; Blau, W. J.; Boland, J. J.; Coleman, J. N. Silver nanowire networks as flexible, transparent, conducting films: Extremely high dc to optical conductivity ratios. *ACS Nano* **2009**, *3*, 1767−1774.
(51) Hossain, M.; Sibin, K. P.; Rao, K. D. M. Angled-stencil lithography based metal mesh/$Ti_3C_2T_x$ MXene hybrid transparent electrodes for low-power and high-performance wearable thermotherapy. *J. Mater. Chem. C* **2021**, *9*, 6257−6267.
(52) Yang, S.; Yan, D. X.; Li, Y.; Lei, J.; Li, Z. M. Flexible poly(vinylidene fluoride)-MXene/silver nanowire electromagnetic shielding films with joule heating performance. *Ind. Eng. Chem. Res.* **2021**, *60*, 9824−9832.
(53) Lipatov, A.; Goad, A.; Loes, M. J.; Vorobeva, N. S.; Abourahma, J.; Gogotsi, Y.; Sinitskii, A. High electrical conductivity and breakdown current density of individual monolayer $Ti_3C_2T_x$ MXene flakes. *Matter* **2021**, *4*, 1413−1427.
(54) Fan, X.; Chen, T.; Dai, L. Graphene networks for high-performance flexible and transparent supercapacitors. *RSC Adv.* **2014**, *4*, 36996.
(55) Gao, Y.; Zhou, Y. S.; Xiong, W.; Jiang, L. J.; Mahjouri-samani, M.; Thirugnanam, P.; Huang, X.; Wang, M. M.; Jiang, L.; Lu, Y. F. Transparent, flexible, and solid-state supercapacitors based on graphene electrodes. *APL Mater.* **2013**, *1*, 012101.
(56) Vangurp, M. The use of rotation matrices in the mathematical-description of molecular orientations in polymers. *Colloid Polym. Sci.* **1995**, *273*, 607−625.

https://doi.org/10.1021/acsnano.2c11180
ACS Nano 2023, 17, 3737−3749